

LANDSCAPE DYNAMICS

Hundred million years of landscape dynamics from catchment to global scale

Tristan Salles^{1*}, Laurent Husson², Patrice Rey¹, Claire Mallard¹, Sabin Zahirovic¹, Beatriz Hadler Boggiani¹, Nicolas Coltice³, Maëlis Arnould⁴

Our capability to reconstruct past landscapes and the processes that shape them underpins our understanding of paleo-Earth. We take advantage of a global-scale landscape evolution model assimilating paleoelevation and paleoclimate reconstructions over the past 100 million years. This model provides continuous quantifications of metrics critical to the understanding of the Earth system, from global physiography to sediment flux and stratigraphic architectures. We reappraise the role played by surface processes in controlling sediment delivery to the oceans and find stable sedimentation rates throughout the Cenozoic with distinct phases of sediment transfer from terrestrial to marine basins. Our simulation provides a tool for identifying inconsistencies in previous interpretations of the geological record as preserved in sedimentary strata, and in available paleoelevation and paleoclimatic reconstructions.

Landscape dynamics are the expression of the interplay between tectono-geodynamic processes that deform and modify Earth's surface and its climate, which acts to transfer sediments from sources to sinks, through drainage networks that incise and dissect the landscape into high-frequency elevation patterns. Earth's physiography acts as a key evolving boundary condition for a plethora of geological, climatic, and biological processes and models (1–4). Traditionally, sedimentology, geochemistry, and paleontological studies have been used to decode Earth's paleoelevation. However, available observations from the geological record remain sparse, providing only a low-resolution, spatially and temporally fragmented representation of past physiography and are, to our knowledge, unable to account for past drainage networks, making it difficult to reconstruct the partitioning and distribution of sedimentary basins, geochemical cycles, the flux of nutrients from continents to oceans, and the evolution of global atmospheric and oceanic circulation. To unlock these constraints, we must be able to model—with high levels of detail—the evolution of the Earth's physiography at the global scale and through geological time.

We present a prediction of the past physiography of the Earth at a global scale, at fine resolution [10 km spatially, 1 million years (Myr) in time]. We simulate landscape evolution resulting from erosion and deposition, adjusting the physiography over time by assimilating a long-wavelength paleoelevation reconstruction derived from the geological record and paleontological archives (5) and paleoclimatic

data from a general circulation model (3). Our results are first calibrated using a series of present-day observations. We then extract an ensemble of predictions that we compare with well-documented natural examples of sediments and water fluxes, stratigraphic architecture of sedimentary basins, and estimates of sediment volumes trapped in terrestrial sinks. Our numerical framework integrates the physics of surface processes and provides 100 Myr of high-spatial and temporal resolution physiography and sediment accumulation maps, fundamental in interpreting and modeling Earth's past environmental and biological conditions.

A global landscape and sediment transport geomodel

We developed a modeling framework accounting for geodynamic, tectonic, climatic, and surface processes to perform paleolandscape reconstructions at a global scale. Based on the recently released global landscape evolution model goSPL (6), landscape dynamics are forced with a state-of-the-art paleoelevation reconstruction tied to its plate tectonic model (5), and a series of paleoprecipitation maps (3). We implement a stepwise matching approach (see SM) to assimilate the paleoelevation dataset and estimate uplift rates over time. In this scheme, the envelope of the reconstructed landscape targets the long-wavelength pattern of the paleoelevation reconstruction model. Predictive model outputs from our paleolandscape reconstructions allow us to build high-resolution (~10 km) maps of the physiography and drainage network organization at the global scale (Fig. 1A), making it possible to simulate past sediment and fluvial paleofluxes across drainage networks (Fig. 1B), to estimate both continental and marine sediment accumulations, and to build global three-dimensional (3D) compacted stratigraphic architectures (Fig. 1C).

First, we calibrate our model (table S1) using modern estimates of suspended and bedload transport from the land to the ocean corresponding to ~20 gigatonnes (GT) per year (Fig. 2A) and contributing to >70% of the global sediment flux (7). These global values are similar to those of the Land2Sea database (7), which contain present-day estimates

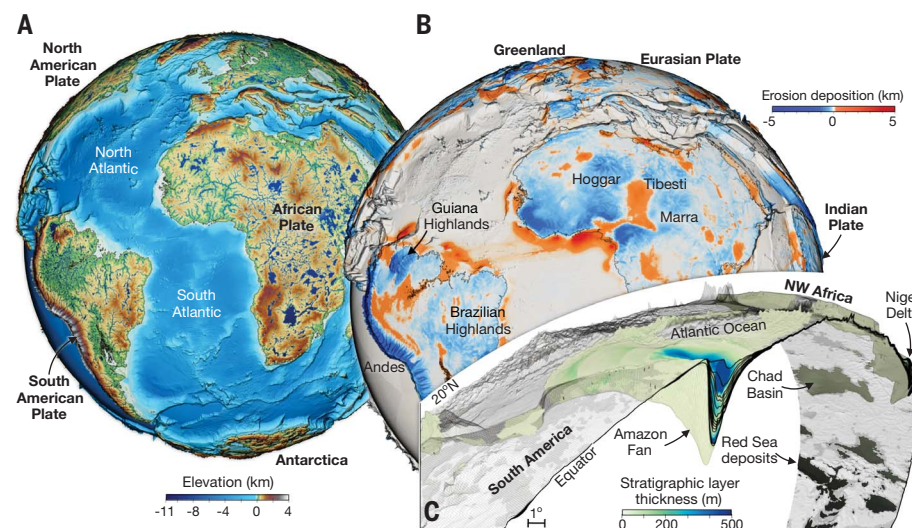


Fig. 1. Landscape evolution simulation. (A) Global physiography and major rivers at 50 Ma, after assimilating paleoelevation (5) and paleoclimatic (3) reconstructions. (B) 50 Myr of cumulative erosion and sedimentation highlighting erosion over mountain ranges (Andes) and topographic highs (Brazilian and Guiana highlands, Hoggar, Tibesti, and Marra) and major sediment accumulations along continental shelves (Atlantic margins) and endorheic basins (Amazonian watershed). (C) Perspective view of a stripe 20° wide featuring the relief and stratigraphy after 100 Myr of evolution; the architecture of the Amazon Fan and other sedimentary basins prominently appear.

¹School of Geosciences, The University of Sydney, Sydney, Australia. ²CNRS, ISTerre, Université Grenoble-Alpes, Grenoble, France. ³ENS, PSL Research University, CNRS UMR 8538, Paris, France. ⁴Université Lyon 1, LGL-TPE, Villeurbanne, France.

*Corresponding author. Email: tristan.salles@sydney.edu.au

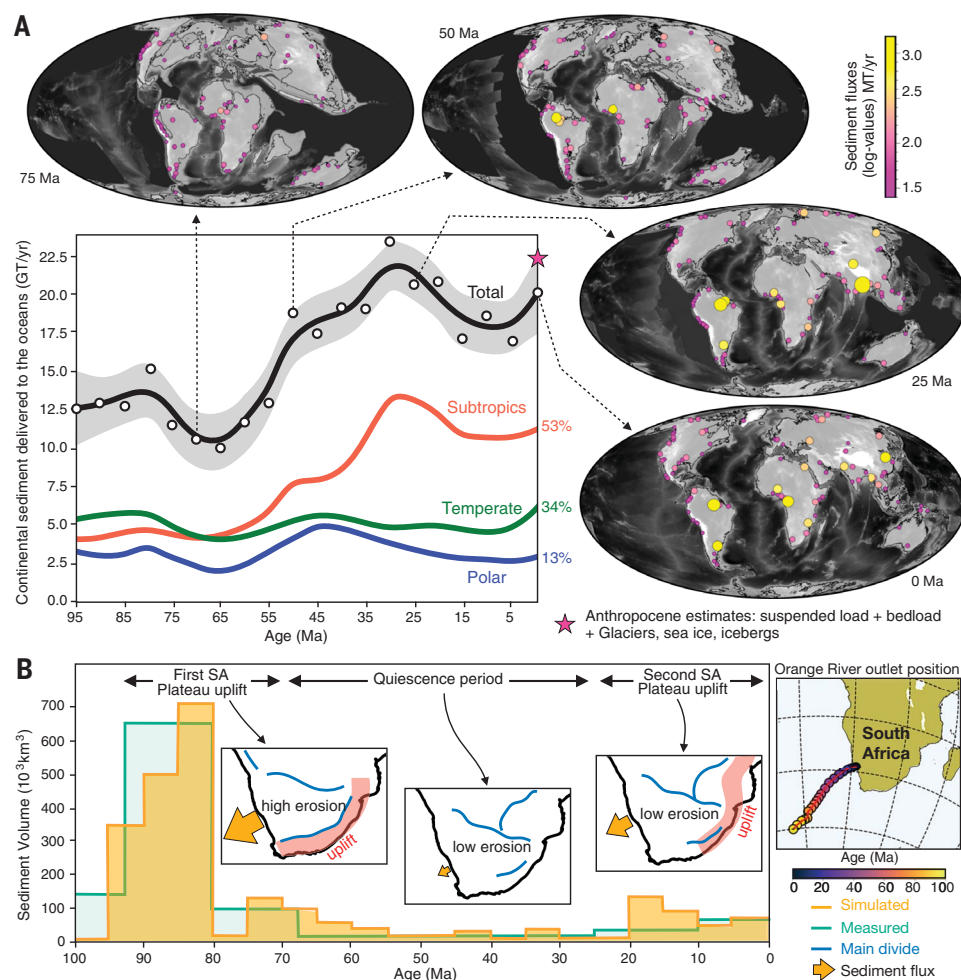


Fig. 2. Sediment flux over time. (A) Map view (pink and yellow circles) of the 100 highest river sediment fluxes at specific times caused by riverine and hillslope processes activated by the interplay between tectonic and climatic forcings. Latitudinal dependence of the sediment fluxes at specific times (circles) and averaged over time (Lowess regression, shaded area corresponds to confidence intervals) (subtropics: from 30°S to 30°N; temperate: 30° to 60°; and polar: above 60°). Stars show the modern estimates of sediment flux to the ocean used for model calibration in magenta (1) and values from the Land2Sea database in pink (7). (B) Computed (orange area) and observed (teal line) sediment fluxes in the Orange River, southern Africa over the past 100 Ma. Inset sketches show the erosion-sedimentation evolution from (29). Map on the right shows the Orange River mouth position reconstructed from the plate motion model (5).

for suspended sediment flux average to 18.6 GT per year based on 1519 exorheic river drainage basins (7). Latitudinal sediment flux distribution shows predominant contributions from subtropical regions corresponding to 53% of the total flux. This strong correlation between sediment flux and climate matches estimates from the global terrestrial sink catchment database (8) and organic carbon flux studies (9). From the multiple flow drainage method used to integrate runoff over the upstream drainage basin area (6), simulated major river positions and associated watersheds conform with those of the real world (Fig. 3A). As an example, the simulated catchment area for the Paraná Basin at the present day, after 100 Myr of simulation, has a similar shape and is only 8% smaller than the actual Paraná catchment (model resolution impedes reconstructing the highest frequencies of river sinuosity). The output also compares well with observed magnitude of discharge for the largest modern rivers (Fig. 3B) and accounts for the discharge-area scaling relationship (exponent close to 1.0 from curve fitting analysis) (10).

The positions of the rivers and their associated catchments are not fixed and evolve over

time (Fig. 3A and fig. S6). At the catchment scale, our simulation can be used to further evaluate the transient geomorphic response of individual catchments to tectonic and climatic forcing (11, 12). As an example, the main tributaries for the Paraná Basin (Grande, Paraguay, Salado, and Uruguay rivers) and their confluence positions are also well-reproduced in the simulation (Fig. 3C). From the longitudinal profiles, we identify several knickzones (Fig. 3C), the amplitudes and positions of which follow observations (13, 14)—particularly for the simulated Uruguay River, which reproduces two knickzones between 1200 and 2000 km (at ~400 and 600 m elevation) similar to the present-day river profile.

Finally, our simulation also reproduces the first-order distribution of the main depocenters for the past 100 Myr (Fig. 1, B and C, Fig. 4, and fig. S10). Comparison with present-day total marine sediment thickness grid GlobSed (15) shows that our simulation underpredicts global thickness by 1.5 km (fig. S7, A and C), which is expected as the cumulative depositional record from this dataset spans a much longer period than ours. However, we find a better match in subtropical regions (0.8 km)

where many of the largest modern oceanic sedimentary basins formed over the past 100 Myr. As an example, it predicts a maximum accumulation under the outer Pakistan shelf of up to 7.5 km in the Indus Fan (fig. S7B) that compares well with the global depocenter observed from subsurface observations (16). Likewise, the predicted accumulation of sediments in the post-Paleocene Bengal Fan (up to 10.3 km fig. S7B) conforms to the geological record (17). Similar observations can be made for the Niger Delta that accumulates in our simulation—up to 9.5 km of sediments, which can readily be compared with the 8.5-km estimate from sediment budgets (18) or the Eromanga Basin in central Australia with a predicted broad 1.2-km thick deposit, also within the range of observed values since the Late Cretaceous (Fig. 5B) (19). For the Amazon Fan (Fig. 1A), we obtain a deposit that extends up to 600 km seaward and records a 13-km thick accumulation that here again matches observations (20).

Water and sediment flux through space and time

The transfer of eroded sediments from the mountains to the oceans is a proxy for long-term

physical weathering and plays a central role in modulating ocean chemistry, and more generally in geochemical cycles over geological time scales (1, 8, 21, 22). We extracted the top hundred largest sediment fluxes (Fig.

2A) and monitored water discharges over the past 100 Myr (Fig. 3A). The distribution of the water discharge, whether dominated by a few major catchments or many smaller watersheds (Fig. 3A and S6), depends on the

size of the river catchments and the amount of rainfall they receive. Typically, the highest sediment fluxes correspond to the largest river discharges. However, this relationship does not always hold because the local physiography

Fig. 3. Water discharges and catchment dynamics. (A) Map view of the 100 largest annual river discharges (circle sizes and colors scale with water flux) and 50 largest drainage basins (gray shading). (B) Modeled water discharge against basin drainage area (white circles) at present day (log scales). Red line, power law curve fitting. Black circles correspond to observed river fluxes at the present day for rivers whose discharge is <2000 m³ per s (horizontal line at ~63 km³ per yr) (1). Paraná drainage basin and tributaries. Simulated longitudinal main rivers profiles (solid curves) and corresponding actual river profiles (dashed, downsampled at 10 km resolution from 90 m SRTM database) (14). (C) Teal lines show identified kickzones for the Uruguay River.

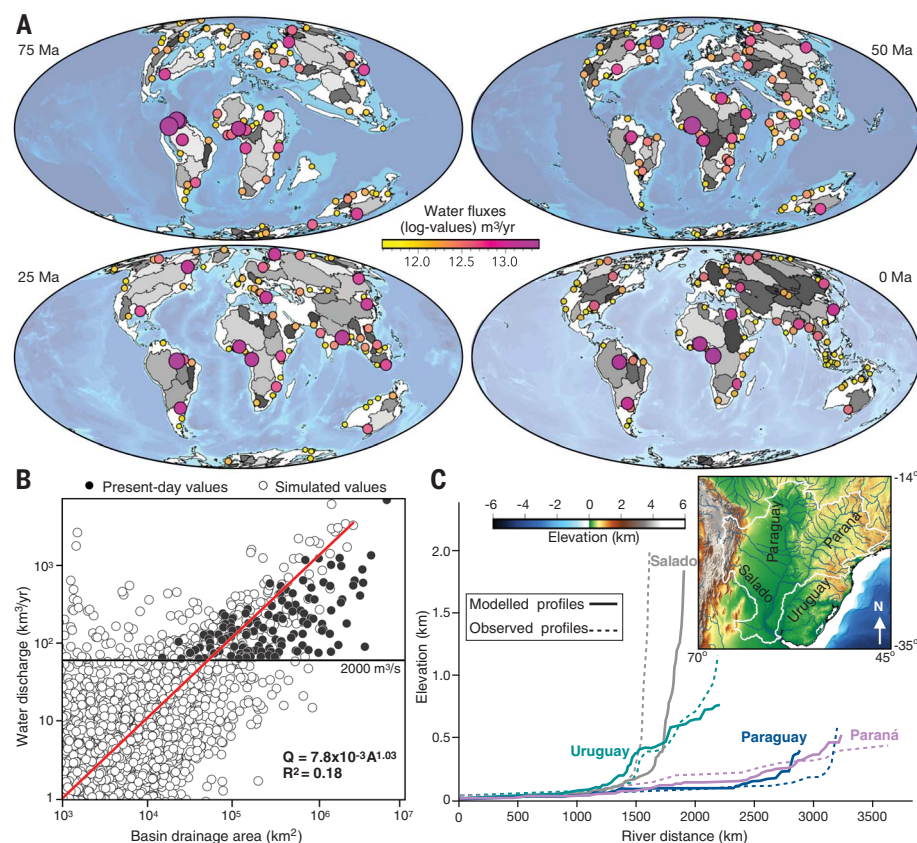
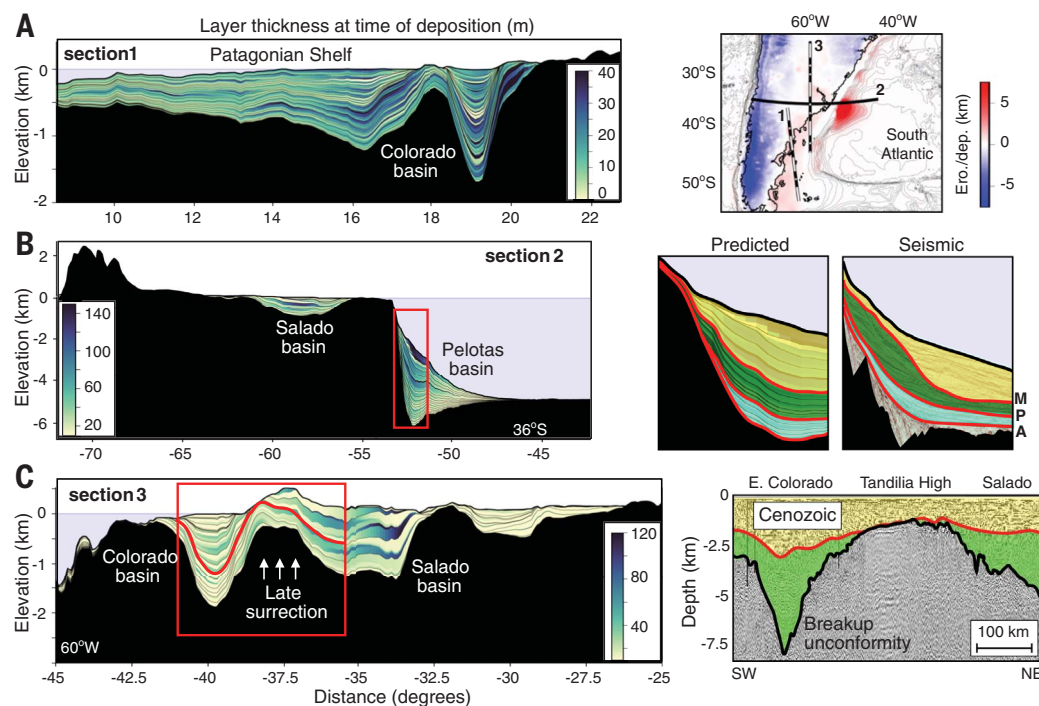


Fig. 4. Stratigraphic predictions.

(A) Cumulative erosion/deposition (top right) at the present day, sliced with three cross sections. Simulated stratigraphy sampled every 1 Myr are displayed and colored by sediment accumulation rates (meters per million years) for each cross section. (B) Predicted stratigraphy for section 2 after 100 Myr of simulation (left) and focus on the Pelotas Basin (right) where comparison with megasequences from 2D seismic sections are presented (34). Red lines in the predicted and interpreted seismic defines the Albian (A ~100 Ma), Paleocene (P ~59 Ma), and Miocene (M ~23 Ma) transitions. (C) Cross section across the Salado and Colorado basins (left) compared with depth-converted interpreted seismic (36). Red line corresponds to the top Cretaceous horizon (~66 Ma) in both panels.



plays a crucial role in modulating sediment flux (21). For example, small catchments adjacent to high mountain ranges, such as on the western side of the Andes, have low water discharges but deliver a large volume of sediments to the ocean (8, 21). Conversely, the northern part of South America or Central Africa at 75 Ma or Southeast Asia at 25 Ma (Fig. 3A) demonstrate that large water flux does not necessarily convey large sediment flux (Fig. 2A). This can either be attributed to high precipitation rates over relatively flat landscapes or to the storage of sediments in upstream depocenters (Fig. 5A).

Both water and sediment fluxes over time mirror several phases of continental scale drainage reorganizations. For example, our reconstruction at 75 Ma suggests that drainage networks in the upper part of the Amazon Basin were feeding an epicontinental sea at the foot of the northern Andes (Figs. 2A and 3A). In our simulation, rearrangement of these fragmented catchments into an Amazon basin that resembles the modern one occurs first around 50 Ma (fig. S9 and movie S3), followed by periods of intermittent flooding and shallow-water sedimentation in mega lakes covering the central part of the basin (movie S3). The complete drainage reversal of the Amazon River, driven by the paleoelevation reconstruction (5), happens during the past 20 Myr in agreement with the geological record that suggests the drying up of the Pebas system due to dynamic uplift during the Miocene epoch (23, 24).

At the catchment scale we evaluate the temporal evolution of the Orange River drainage basin in southern Africa (Fig. 2B). The surface uplift history of this cratonic interior region has been attributed to mantle processes (25). Such regional settings, distant from plate boundaries and with negligible effects from crustal tectonics, comprise most continental areas. However, the mechanisms driving their long-term denudation patterns as well as their contributions to global sediment flux are unclear (26, 27). The modeled sediment flux shows good agreement with observations (28, 29); specifically, the simulation reproduces the magnitude and timing of phases of high sedimentation rates during the Late Cretaceous (93.5 to 81 Ma) and from the Oligocene to the present day (29).

The simulation predicts an almost twofold increase in bulk detrital flux to the oceans during the Cenozoic (Fig. 2A). The main sediment contribution comes from subtropical rivers with a threefold increase from 5 to 15 GT per year between 60 and 30 Ma. This increase is associated with the rise of the Himalayas and Tibetan plateau and to the early rearrangement of the Amazon paleobasin. Similar conclusions have been drawn when interpreting the general increase in seawater strontium isotopic composition over the past 100 Myr,

with the Late Cenozoic rise of the Himalayas as its paroxysmal expression (30). Our results also show an increase in sediment flux delivered to the oceans over the past 15 Myr mainly from rivers in temperate regions (Fig. 2A). This increase has already been documented (22, 27) but its origin remains unclear as the cooling climate during the Late Cenozoic should result in decreasing erosion rates as wetter and warmer climates accelerate mechanical rock weathering (31). Under these conditions, enhanced Pleistocene glacial erosion has been invoked as a major driver (27, 32). Our model does not account for glacial erosion and therefore the simulated increase represents the lower range of sediment flux estimates. It shows a net positive contribution from riverine processes during the past 10 Myr (~2 GT per year representing

a ~10% increase in incoming flux) that must be considered when assessing global long-term erosion rates. However, this late increase is relatively limited and the average flux over the Neogene remains relatively stable (~18.5 GT per year).

Our method offers an independent alternative to existing approaches evaluating sediment flux and long-term trends in erosion rates (22, 27) such as Be isotope ratios or thermochronometric data. Similar to these approaches, our results suggest that sediment flux were higher than what they seem from the preserved sediment record (likely induced by observational biases, also known as the Sadler effect) and provide limited evidence for any major changes in worldwide erosion rates over the Late Cenozoic (26, 27).

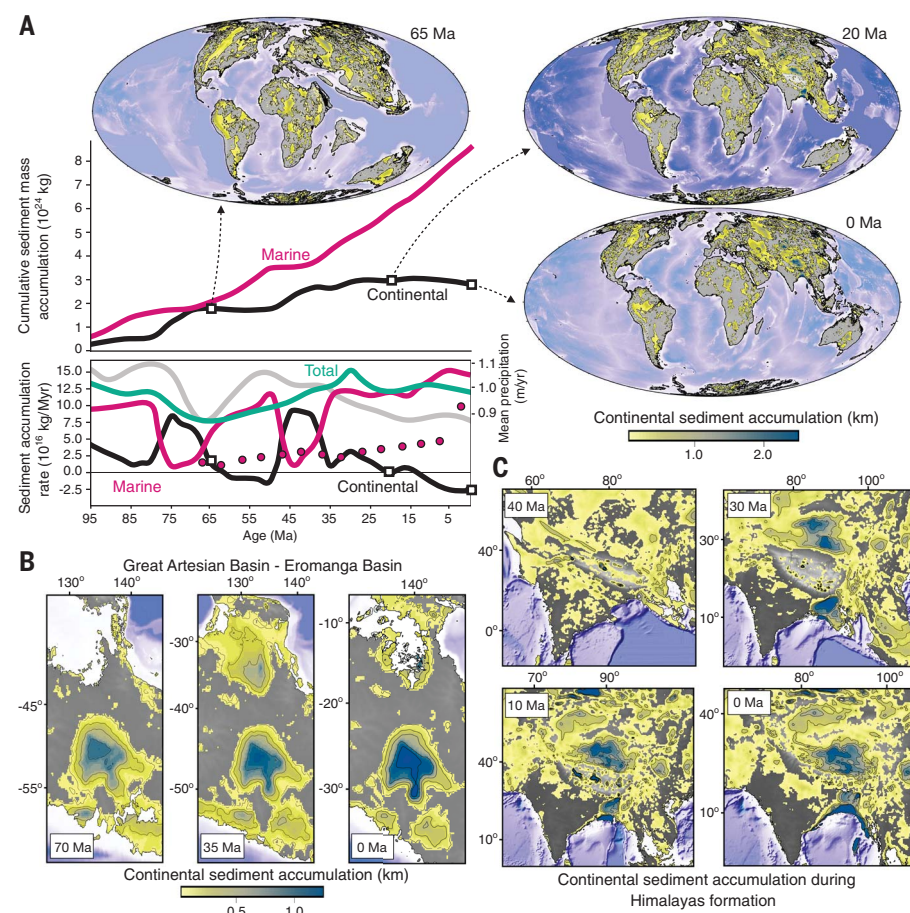


Fig. 5. Continental sediment cover temporal evolution. (A) Predicted temporal evolution of marine (magenta line) and continental (black line) cumulative sediment mass accumulation (top) and rate (bottom) assuming an average grain density of 2.7 g/cm^3 (total rate in teal). Magenta circles indicate estimated global values for ocean basins (26). The gray curve shows the average precipitation from the paleoclimate reconstruction (3). Maps show distribution of continental depocenters at 65, 20, and 0 Ma. (B) Predicted sediment accumulation in the Eromanga Basin (central Australia) showing up to 1.5 km of sediments underlying the endorheic Lake Eyre basin. (C) Predicted sediment accumulation in, during, and after the India-Eurasia collision. Note the formation of the Himalayan foreland basin in the south (between the Himalayan belt and the Indian continental shield) and the filling of the Tarim and Qaidam basins along the northern margin of the Tibetan plateau.

Oceanic and continental sedimentary basins

Our framework captures, at first order, the details of sedimentary basin architectures. Here, we focus again on South America (Fig. 4) and compare cross sections of the predicted stratigraphy and sediment accumulation maps with post-rift sediment thicknesses imaged by seismic data. Section 1 crosses the Colorado Basin on its northern side where the model records up to 1.8 km of sediment accumulation followed by continuous and relatively thin layers extending across the Patagonian Shelf (Fig. 4A). The simulated stratigraphic architecture of the shelf agrees with large-scale elongated stratigraphy imaged by seismic data (33). For section 2, the main deposits are characterized by a seaward thickening sedimentary wedge, with two depocenters that match the location, thickness, and stratigraphic record of the Salado and Pelotas basins (34, 35) (Fig. 4B). Section 3 cuts through the large alluvial plain of the Paraná Basin on its northern side, where it predicts ~250 m of post-rift sediment accumulation, before entering first the Salado then the Colorado basins. In addition, our simulation predicts an early connection (up to 45 Ma) between these basins and a late tectonic forcing that uplifted the southern side of the Salado Basin by 500 m. This, however, is partly at odds with the current understanding of the tectonic and sedimentary evolution of the region (34, 36). This mismatch corroborates identified inconsistencies in Late Cretaceous paleoelevation reconstructions when compared with fossil collections (37, 38). It illustrates how quantitative metrics extracted from our approach could be used to test existing paleogeographic reconstructions. To adjust the paleoelevation reconstruction, one option consists of extending eastward the orographic belt of the Tandilia System during the early stages of the simulation until the predicted stratigraphic record matches the subsurface archive (37).

Continental sediments modulate the geological carbon cycle through weathering (39). As such, investigating the spatial and temporal evolution of terrestrial sinks is crucial to refining our understanding of Earth's paleoclimate variability. In contrast to marine deposits on continental margins, for which overall net deposition and good stratigraphic control exist (15), terrestrial sedimentary basins are typically less complete due to sedimentary erosion and hiatuses and are much harder to correlate between basins (8). From our simulation, we estimate the temporal evolution of endorheic (internally drained) and exorheic (coastal) continental sinks (Fig. 5A) and find that terrestrial deposits store some 28% of the total sedimentary yield over the past 100 Myr. We predict a two-stage increase, first between 80 and 60 Ma during the drying of the North America interior seaway (5), partial sedimentary

filling of Andean retroarc foreland basins (40), and to a lesser extent, the transition from marine to fluvial lacustrine environments of the epicontinental Eromanga Sea (19) (Fig. 5B). The second, between 50 and 25 Ma, is triggered by the Himalayan orogeny and the development of extensive foreland basins (16, 17) and the filling of large endorheic basins north of the Tibetan plateau (Fig. 5C). We find that global sediment accumulation rates are relatively constant over the past 100 Myr with an average value of 11.5×10^{16} kg per Myr (ranging between 7.6 and 15.0×10^{16} kg per Myr, Fig. 5A). It supports the null hypothesis (27) that suggests a limited impact of global climate change and mountain building events on the long-term global sedimentation rate (41). Despite its overall global stability, the analysis of individual contribution from either marine or continental regions tells a more complex history related to the fine balance between physiography development, sediment transport, and deposition (Fig. 5A). Over the Late Cenozoic (from 30 Ma), we predict a long-term decrease in preserved continental sediment volume. Negative rates in Fig. 5A represent erosive periods (particularly along continental margins) that translate into stratigraphic hiatuses and explain the observed mismatch between estimated and simulated sediment accumulation rates (Fig. 5A). We first relate this long-term continental decrease to limited accommodation space in major endorheic basins due to rapid infilling by sustained erosion before the Oligocene-Eocene transition. This infill is concomitant with the development of major continental-scale drainage systems throughout the Miocene (such as the Amazon, Ganges-Brahmaputra, or Indus river basins Figs. 3A, 5C, and fig. S7B) that wash out sediments from the surface of continents. In addition, the Oligocene-Eocene transition marks the emergence of continental shelves which become prone to continental erosion and increase sediment transfer to the marine environment (41). Our results not only highlight the critical role played by the sediment routing systems in modulating long-term sediment fluxes at the global scale but also offer a new perspective on the apparent discrepancy between Late Cenozoic stability of global erosion rates (27) and the observed increase in marine sedimentation (22, 30).

Conclusion

We have built a quantitative and integrated exploratory modeling framework that provides global predictions of physiographic changes at 10 km and 1 Myr resolution. This time-lapse view of the Earth's landscapes is tightly linked to its associated global stratigraphy for the past 100 Myr. Our simulations yield suites of continuous, high-resolution global elevation and erosion/deposition accumulation maps, as well as water and sediment fluxes and

stratigraphic information that form the basis for estimating the rates at which the global landscape changes. This dataset permits testing of the responses of the Earth's surface to different hypotheses related to climate, tectonics, and paleogeography. In addition, our model reproduces the key components of source-to-sink systems from catchment dynamics depicting river networks over time, to marine and continental sedimentary basin evolution under various forcing conditions. This analysis permits better quantification of the role that the constantly evolving physiography of the Earth has played in modulating the transport of sediments from mountain tops to ocean basins, ultimately regulating the carbon cycle and Earth's climate fluctuations through deep time. Exploring these results in tandem with the geological record will permit testing of long-standing hypotheses regarding first order features of the Earth system, such as biogeochemical cycles or biological evolution. The approach can also help to identify inconsistencies in our understanding of the origin and evolution of particular sedimentary strata and to pose alternative hypothesis that could be tested with, for example, new thermochronological or stratigraphic data in certain model-highlighted locations.

REFERENCES AND NOTES

1. J. P. Syvitski, S. D. Peckham, R. Hilberman, T. Mulder, *Sediment. Geol.* **162**, 5–24 (2003).
2. E. Straume, C. Gaina, S. Medvedev, K. Nisancioglu, *Gondwana Res.* **86**, 126–143 (2020).
3. P. Valdes, C. Scotese, D. Lunt, *Clim. Past* **17**, 1483–1506 (2021).
4. O. Hagen *et al.*, *J. Biogeogr.* **46**, 1792–1807 (2019).
5. C. Scotese, N. Wright, PALEOMAP Paleodigital Elevation Models for the Phanerozoic (2018); https://www.earthbyte.org/webdav/ftp/Data_Collections/Scotese_Wright_2018_PaleoDEM/Scotese_Wright2018_PALEOMAP_PaleoDEMs.pdf.
6. T. Salles, C. Mallard, S. Zahirovic, *J. Open Source Softw.* **5**, 2804 (2020).
7. B. Peucker-Ehrenbrink, *Geochim. Geophys. Geosyst.* **10**, 6 (2009).
8. B. Nyberg, R. Gawthorpe, W. Helland-Hansen, *Geomorphology* **316**, 1–23 (2018).
9. W. Ludwig, J.-L. Probst, S. Kempe, *Global Biogeochem. Cycles* **10**, 23–41 (1996).
10. K. Whipple, G. Tucker, *J. Geophys. Res.* **104**, 17661–17674 (1999).
11. J. Perron, L. Royden, *Earth Surf. Process. Landf.* **38**, 570–576 (2013).
12. B. A. Adams, K. X. Whipple, A. M. Forte, A. M. Heimsath, K. V. Hodges, *Sci. Adv.* **6**, eaaz3166 (2020).
13. A. G. Lima, A. L. Binda, *J. S. Am. Earth Sci.* **48**, 262–270 (2013).
14. V. Rodríguez Tribaldos, N. J. White, G. G. Roberts, M. J. Hoggard, *Geochim. Geophys. Geosyst.* **18**, 2321–2353 (2017).
15. E. O. Straume *et al.*, *Geochim. Geophys. Geosyst.* **20**, 1756–1772 (2019).
16. P. Clift, *Prog. Earth Planet. Sci.* **4**, 39 (2017).
17. M. Blum *et al.*, *Sci. Rep.* **8**, 7973 (2018).
18. J.-L. Grimaud, D. Rouby, D. Chardon, A. Beauvais, *Basin Res.* **30**, 169–186 (2018).
19. C. Braz *et al.*, *Basin Res.* **33**, 3378–3405 (2021).
20. M. Rodger, A. Watts, C. Greenroyd, C. Peirce, R. Hobbs, *Geology* **34**, 1081–1084 (2006).
21. J. D. Milliman, J. P. M. Syvitski, *J. Geol.* **100**, 525–544 (1992).
22. P. Molnar, *Annu. Rev. Earth Planet. Sci.* **32**, 67–89 (2004).

23. G. Shephard, L. Liu, D. Müller, M. Gurnis, *Gondwana Res.* **22**, 658–663 (2012).
24. N. Flament, M. Gurnis, D. Müller, D. Bower, L. Husson, *Earth Planet. Sci. Lett.* **430**, 9–18 (2015).
25. J. R. Stanley, R. M. Flowers, *Lithosphere* **12**, 74–87 (2020).
26. J. K. Willenbring, F. von Blanckenburg, *Nature* **465**, 211–214 (2010).
27. J. Willenbring, D. Jerolmack, *Terra Nova* **28**, 11–18 (2015).
28. J. Stanley *et al.*, *Journal of Geophysical Research: Solid Earth* **126**, e2020JB021243 (2021).
29. G. Baby, F. Guillocheau, J. Braun, C. Robin, M. Dall'Asta, *Terra Nova* **32**, 53–65 (2020).
30. J. M. Edmond, *Science* **258**, 1594–1597 (1992).
31. M. C. Eppes *et al.*, *Geophysical Research Letters*, **47**, 2020GL089062, (2020).
32. M. Koppes *et al.*, *Nature* **526**, 100–103 (2015).
33. J. Cavallotto, R. Violante, F. Hernández-Molina, *Biol. J. Linn. Soc.* **103**, 346–362 (2011).
34. B. Conti *et al.*, *Mar. Pet. Geol.* **83**, 1–25 (2017).
35. U. Schattner, F. J. Lobo, A. López-Ouirós, J. L. Nascimento, M. Mahiques, *Basin Res.* **32**, 293–301 (2019).
36. J. Lovecchio *et al.*, *Terra Nova* **30**, 359–368 (2018).
37. M. J. Arrouy *et al.*, *Sci. Rep.* **6**, 30590 (2016).
38. W. Cao *et al.*, *Biogeosciences* **14**, 5425–5439 (2017).

39. J. Krissansen-Totton, D. C. Catling, *Nat. Commun.* **8**, 15423 (2017).
40. M. C. Menegazzo, O. Catuneanu, H. K. Chang, *Mar. Pet. Geol.* **73**, 131–156 (2016).
41. R. Schumer, D. Jerolmack, *J. Geophys. Res.* **114**, F00A06 (2009).

ACKNOWLEDGMENTS

This research was undertaken with resources from the National Computational Infrastructure supported by the Australian Government and from Artemis HPC supported by the University of Sydney. We would also like to thank the two anonymous reviewers for their suggestions and comments. **Funding:** This work was supported by the following: Australian Research Council grant IC190100031 (to T.S.) and Australian Research Council grant DE210100084 (to S.Z.) **Author contributions:** Conceptualization: T.S. and L.H. Methodology: T.S. and L.H. Investigation: T.S. and L.H. Visualization: T.S. and L.H. Funding acquisition: T.S. and S.Z. Project administration: T.S. Supervision: T.S. Writing – original draft: T.S., L.H., P.R., N.C., and M.A. Writing – review and editing: T.S., L.H., P.R., N.C., M.A., S.Z., C.M., and B.H.B. **Competing interests:** Authors declare that they have no competing interests. **Data and materials availability:** The scientific software used in this study, goSPL (13), is available from <https://github.com/Geodels/gospl> and the software documentation can be found at <https://gospl.readthedocs.io>. We also provide a series of Jupyter notebooks used for pre-and post-processing model outputs and

can be accessed at <https://github.com/Geodels/gospl-global-workflows>. The PALEOMAP paleoelevation reconstruction and related GPlates rotation and geometry files are downloaded from <https://www.earthbyte.org/paleodem-resource-scotese-and-wright-2018>. Paleoprecipitation maps from the HadCM3BL-M2.1aD model (3) are available at <https://www.paleo.bristol.ac.uk>. Simulation results provided as netcdf files containing four parameters: elevation, filled flow accumulation (rivers with lakes), flow accumulation (rivers only) and watershed (drainage basins) are available at 5 Myr interval from <https://osf.io/5aek4/>.

License information: Copyright © 2023 the authors, some rights reserved; exclusive licensee American Association for the Advancement of Science. No claim to original US government works. <https://www.sciencemag.org/about/science-licenses-journal-article-reuse>

SUPPLEMENTARY MATERIALS

science.org/doi/10.1126/science.add2541

Materials and Methods

Figs. S1 to S11

Table S1

Movies S1 to S3

References (42–72)

Submitted 2 June 2022; accepted 12 January 2023
10.1126/science.add2541